*Center for Turbulence Research*
*Proceedings of the Summer Program 2006*



# Numerical investigation and preliminary modeling of a turbulent flow over a multi-perforated plate

**By S. Mendez†, J. Eldredge‡, F. Nicoud¶, T. Poinsot‖, M. Shoeybi AND G. Iaccarino**

Wall-resolved Large-Eddy Simuations (LES) of a turbulent flow around a multi-perforated plate are presented. Periodic conditions are used in both directions tangential to the plate so that only one or a few micro-jets are computed. Comparisons between one and four holes computations show that single-hole domain calculations allow the capture of the essential characteristics and statistics of the flow. The results from two different numerical codes and strategies also compare favorably with the existing experimental data in the case of a large-scale cold flow with effusion. The overall quality of the simulations being established, further analysis of the flow structure is performed. Two results relevant to further modeling studies are obtained: the jet angle somewhat departs from the hole angle, and the velocity profile in the jet is highly inhomogeneous with a strong recirculation zone in the downstream side. Preliminary testing of a simple dynamic model for the normal velocity is also presented. A robust algorithm for implementing this model in coupled computational domains is developed. Deficiencies in the model are identified and discussed.

## 1. Introduction

In almost all the systems where combustion occurs, solid boundaries need to be cooled. In gas turbines, one often uses multi-perforated walls to produce the necessary cooling (Lefebvre 1999). In this approach, fresh air coming from the casing goes through the perforations and enters the combustion chamber. The associated micro-jets coalesce and produce a film that protects the internal wall face from the hot gases (Goldstein 1971; Yavuzkurt *et al.* 1980). The number of submillimetric holes is far too large to allow a complete description of the generation/coalescence of the jets when computing the 3-D turbulent reacting flow within the burner. Effusion is however known to have drastic effects on the whole flow structure, noticeably by changing the flame position. Consequently, there is a need to better understand the effects of effusion on the turbulent flows and to take them into account when performing full-scale Reynolds-Averaged Navier–Stokes (RANS-) or LES-type calculations for design purposes.

Due to technological difficulties, measurements prove highly challenging in the vicinity of multi-perforated plates so that Direct Numerical Simulation (DNS) or wall-resolved LES are methods of choice to gain insights into the effects of effusion on the turbulent boundary layer. However, the CPU time required for performing such simulations of a classical case with hundreds of jets would be prohibitive. Two different numerical procedures were recently proposed and tested (Mendez *et al.* 2005a,b), the computational

† CERFACS, Toulouse, France
‡ Mechanical and Aerospace Engineering Department, University of California, Los Angeles
¶ Applied mathematics, University Montpellier II, France - nicoud@math.univ-montp2.fr
‖ CNRS IMF Toulouse, France

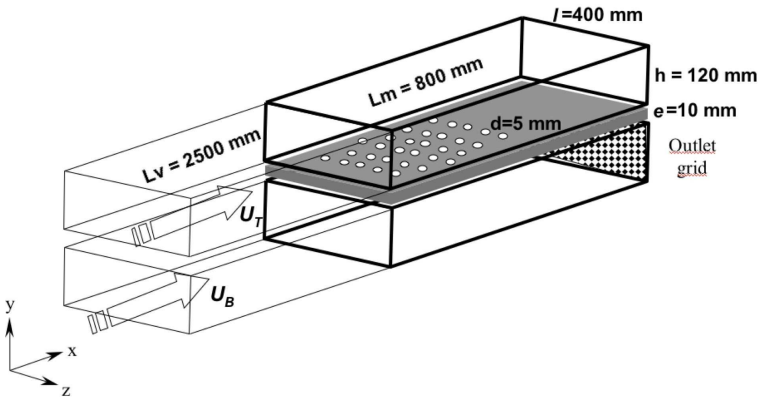


FIGURE 1. Principle of the large-scale isothermal "LARA" experiment.

domain containing one single perforation, periodic conditions being imposed along the tangential directions to mimic an infinite plate. Both approaches gave results in fair agreement with the velocity measurements from a large-scale isothermal experimental setup (Miron *et al.* 2005). Still, the implications of using periodic conditions are not fully understood yet.

The objectives of this study are the following:

- assess the influence on the results of computing one single hole bi-periodic domain. This means comparing the existing results (Mendez *et al.* 2005b) with a simulation where the computational domain is twice as large in both tangential directions and analyze the effects of the enlargement in terms of jet interactions and turbulence length scales,
- compare the numerical results from two different LES codes with different numerical strategies. This will provide a measure of the effects of potential numerical artifacts on the results,
- characterize global flow parameters as the discharge coefficient and the jet angle as well as the general flow structure,
- perform preliminary *a priori*/*a posteriori* tests of basic modeling ideas derived from existing acoustic models for liners.

## 2. Numerical configurations

All the computations presented in this paper are related to the "LARA" experimental setup studied by Miron *et al.* (2005) with a two-component Laser Doppler Velocimeter system. This is a large-scale isothermal experiment whose principle is depicted in Fig. 1. Two attached turbulent boundary layers are generated around a flat plate that contains a multi-perforated section. The pressure in the lower stream being increased by a grid located downstream of the test section, an effusion flow takes place through the perforated section. To allow precise jet structure investigations, the hole diameter in this experiment is $d = 5$ mm (0.5 mm is the common value for gas turbines applications). The spacing between the holes corresponds to classical industrial applications: the distance between two consecutive rows is 3.37 diameters in the spanwise direction and 5.84 diameters in the streamwise direction. Due to the staggered disposition of the perforations, the hole-to-hole distances are respectively $2 \times 3.37$ and $2 \times 5.84$ diameters in the spanwise and streamwise directions. The thickness of the plate is 10 mm and holes are angled at 30° with the plate. The operating point considered in this paper is such that the pressure

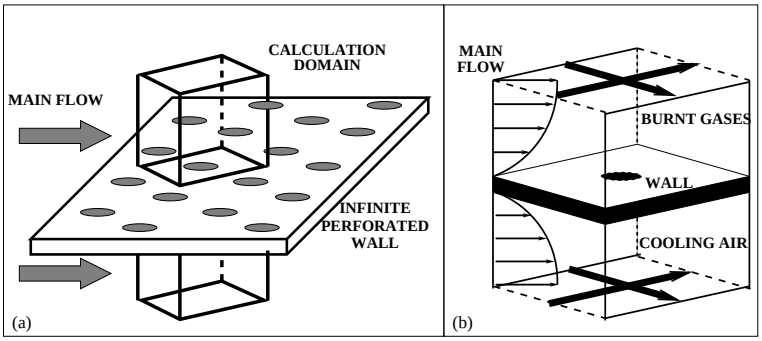


FIGURE 2. From the infinite plate to the "bi-periodic" calculation domain. (a) Geometry of the infinite perforated wall. (b) Calculation domain centered on a perforation; the bold arrows correspond to the periodic directions. The distance between two consecutive holes is in the range of 6–8 hole diameters.

drop across the plate and blowing ratio (jet-to-"hot" crossflow momentum ratio) are 42 Pa and 1.78, respectively. The Reynolds number for the primary "hot" flow (based on the duct centerline velocity and the half height of the rectangular duct) is $Re_1 = 17750$, while it is $Re_2 = 8900$ for the secondary "cold" flow. The bulk velocity in the "hot" stream is $U_b \approx 4.29$ m/s.

### 2.1. *Small-scale computations*

In order to gain insight into the detailed structure of the turbulent flow through the liner, it is useful to perform small-scale computations (Mendez *et al.* 2005b). For this purpose, the bi-periodic computational domain is designed as the smallest domain that can reproduce the geometry of an infinite plate with staggered perforations (Fig. 2). The main tangential flow at both sides of the plate is enforced by a constant source term added to the momentum equation, as is usually done in channel flow simulations. The effusion flow through the hole is sustained by imposing a uniform vertical mass flow rate at the bottom boundary of the domain. The source terms and uniform vertical mass flow rate were tuned in order to reproduce the operating conditions given in Section 2.

### 2.2. *Large-scale computations*

As discussed later in Section 4, a preliminary model for the flow over the liner has been proposed and implemented in the "CDP" code. Computations of the "LARA" experiment were performed as *a posteriori* testing of this liner model. The computational domain for these calculations is shown in Fig. 3, where the boundary conditions used are also shown. Two identical channels share a common wall, part of which is comprised of a multi-perforated liner. Note that in both channels, the computational domain is periodic in the spanwise direction. The mesh contains approximately $10^6$ hexahedra.

## 3. Numerical results

Two different codes dedicated to LES/DNS in complex geometries have been used to perform the small-scale simulations, namely the "AVBP" (AVBP 2006) and "CDP" (Ham & Iaccarino 2004) codes. The main characteristics of these codes and associated simulations are displayed in Table 1. In this table, $< y^+ >$ is an estimate of the averaged first off-wall point position in wall units, $V_j$ is the bulk velocity in the hole, and $C_D$

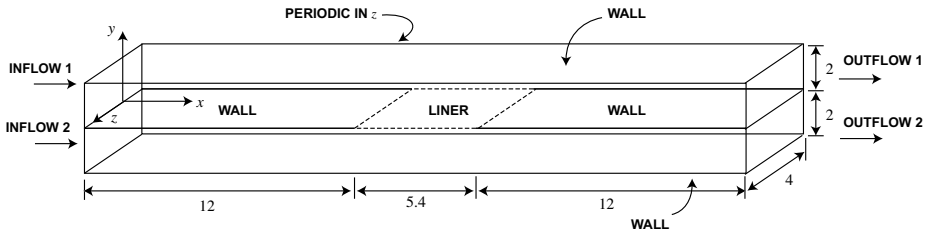


FIGURE 3. Large-scale computational domain for the *a posteriori* testing of the liner model.

| Run | Code | equations | Order of accuracy | mesh | $< y^+ >$ | $V_j$ (m/s) | $\Delta P$ (Pa) | $C_D$ |
|---|---|---|---|---|---|---|---|---|
| AVBP-1H | AVBP | compressible | 3rd | 1.5 M tetrahedra | 5 | 5.6 | 41 | 0.66 |
| CDP-1H | CDP | incompressible | 2nd | 1.5 M hexahedra | 1 | 5.6 | 39.5 | 0.67 |
| AVBP-4H | AVBP | compressible | 3rd | 6 M tetrahedra | 5 | 5.6 | 41 | 0.66 |

TABLE 1. Main characteristics of the small-scale simulations

is the discharge coefficient $V_j/\sqrt{2\Delta p/\rho}$. Two kinds of comparisons are discussed in the following subsections:

- AVBP-1H/AVBP-4H comparison: for a given numerical methodology, two simulations with different computational domain sizes are compared in Section 3.1 in order to establish the validity of the one-hole based simulations,
- AVBP-1H/CDP-1H comparison: for a given computational domain and operating point, two simulations performed with two different implementations of the Navier-Stokes equations are compared in Section 3.2 in order to establish that the computed fields are not contaminated by numerical errors.

### 3.1. *Effect of the number of holes*

By making use of a bi-periodic computational domain containing a single hole, one forces the hole-to-hole distance to play a major role in the simulation. Any turbulence length scale greater than half the domain size would not have enough room to appear and, more importantly, jet-to-jet interaction cannot take place. Given that the jet-to-jet distance is only 6–10 hole diameters, basing the study on one-hole bi-periodic computations is a questionable choice. The purpose of this section is to assess how the results are modified, if they are, by this arbitrary choice. To this end, a LES of a bi-periodic computational domain twice as large in each tangential direction has been performed with the AVBP code (Run AVBP-4H in Table 1). The mesh is the same as for the 1-hole computation (Run AVBP-1H in Table 1), duplicated four times. In order to save CPU time, the initial condition for this 4-hole computation is a four-times duplicated version of an established solution from the 1-hole simulation. Figure 4 shows the time evolution of the streamwise velocity at four sensors located 1 diameter above each of the four computed holes. As expected, they initially behave similarly and after approximately two flow-through times (FTT), the instantaneous evolutions become different from one jet to the other. Note that

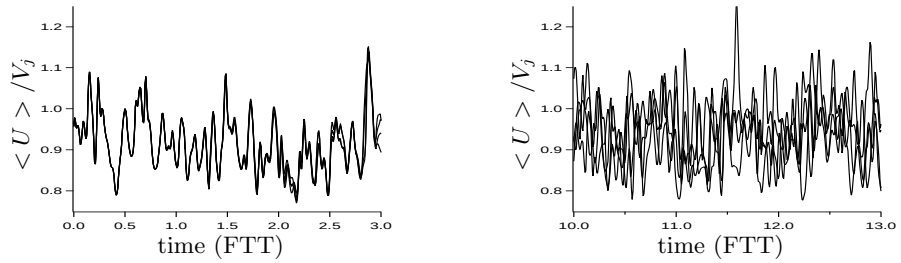


FIGURE 4. Time evolution of the streamwise velocity one diameter above the four holes in the "hot" stream. Left: beginning of the run, Right: after the transitional phase.

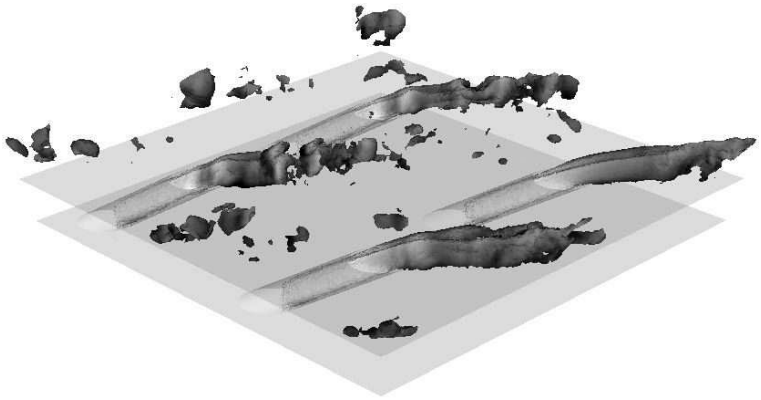

FIGURE 5. Instantaneous iso-surface of velocity modulus (1.125 $V_j$) colored by the normal velocity component (scale is from $-0.18$ $V_j$ (black) to 0.71 $V_j$ (white)) for the AVBP-4H run.

the FTT is based on the jet-to-jet streamwise distance and bulk velocity in the primary flow, while the length and velocity scales chosen for most of the plots in the paper are the hole diameter $d$ and hole bulk velocity $V_j$. The statistics discussed in the remainder of this section have been obtained over 10 FTT, while the accumulation process started at 13 FTT. It is assumed that any jet-to-jet interaction would have had enough time to appear during the total of 23 FTT that were computed. Since a detailed analysis of the snapshots over the simulation showed no such event, it is believed that the micro-jets are not subject to collective interaction, at least for the operating point considered in this study.

A typical snapshot of a velocity iso-surface is depicted in Fig. 5, which shows that the four jets do not have the same appearance. Some seem very quiescent, with a laminar type of velocity iso-surface, others are characterized by an intense vortex- shedding process (see the most downstream and the most upstream jets in Fig. 5), while the foreground jet shows an intermediate behavior. Note that these two types of states can be found alternatively in any of the computed jets, which is expected since they are all statistically equivalent. The same intermittent behavior is found in the 1-hole simulation as shown in Fig. 6, which displays the same iso-velocity surface at different times over the simulation.

In terms of statistics, the 1-hole and 4-hole configurations also lead to very similar results. This is illustrated in Figs. 7 and 8, where the profiles of the averaged and root mean square (rms) of the streamwise and normal velocity components are shown for two locations downstream of the hole. In these plots the profiles corresponding to the four holes of the 4-hole computation are represented by the same line type since there is no

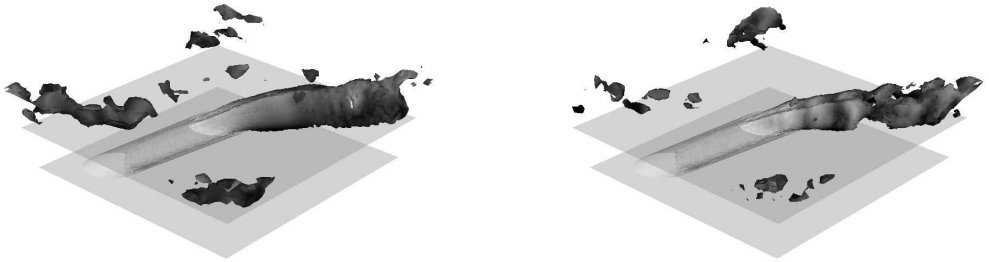

FIGURE 6. Instantaneous iso-surface of velocity modulus (1.125 $V_j$) colored by the normal velocity component (scale is from $-0.18$ $V_j$ (white) to 0.71 $V_j$ (black)) for the AVBP-1H run at two different instants.

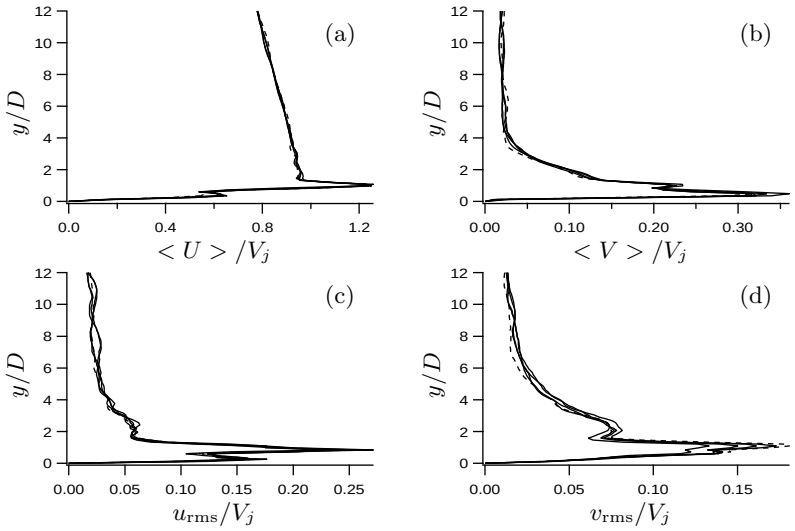


FIGURE 7. Velocity profiles from the AVBP-1H (- - - - ) and AVBP-4H (——— ) computations 2.92 diameters downstream of the hole: (a) time averaged streamwise velocity, (b) time averaged normal velocity, (c) rms of streamwise velocity, (d) rms of normal velocity.

statistical difference between these profiles. The differences observed are due to the lack of statistical convergence and provide an easy way to estimate the statistical incertitude in the plotted profiles. Given this error bound, there is no difference between the 1-hole and the 4-hole computations. The same conclusion was drawn from all the one-point statistics comparisons performed between the two configurations.

Typical streamwise two-point correlations are depicted in Fig. 9 for the streamwise and normal velocity. These profiles were obtained by post-processing 25 independent solutions of AVBP-4H and 62 AVBP-1H snapshots. The four-hole regions in AVBP-4H were subsequently averaged together to obtain the results shown in this figure, which also depicts the position of the reference points for the computation of the streamwise two-point correlations. In one case (Figs. 9a, c) the reference point (which corresponds to zero axial distance in the figure) is located above a hole and the end point is located above the next hole in the downstream direction. In the other case (Figs. 9b, d), the reference point is located at half distance between two consecutive lines of holes. In general, no major difference is present between AVBP-1H and AVBP-4H, supporting the fact that no major artifacts are present in the 1-hole simulation. Note however that

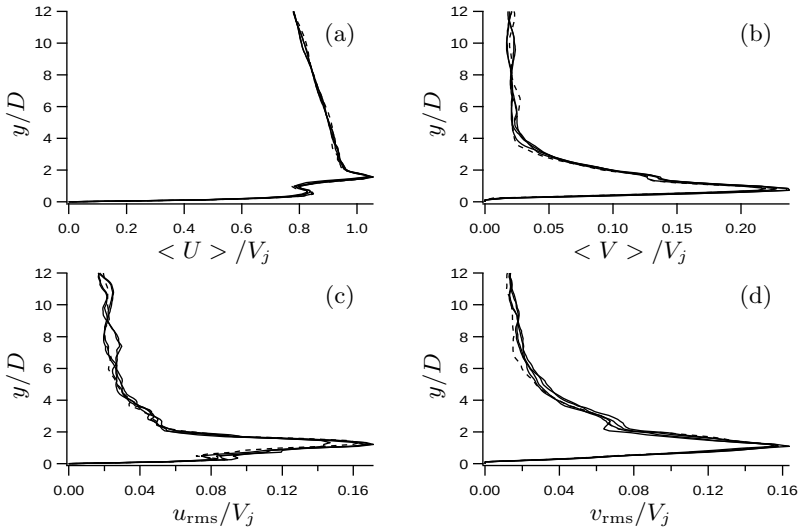


FIGURE 8. Velocity profiles from the AVBP-1H (- - - - ) and AVBP-4H (——— ) computations 5.84 diameters downstream of the hole (viz. in between two consecutive holes in the spanwise or streamwise direction): (a) time averaged streamwise velocity, (b) time averaged normal velocity, (c) rms of streamwise velocity, (d) rms of normal velocity.

non-negligible differences between AVBP-1H and AVBP-4H are present for the normal velocity two-point correlation (Fig. 9c). Given the very good agreement observed previously for instantaneous velocity (Figs. 5 and 6) and for the mean and rms of streamwise and normal velocities (Figs. 7 and 8), this difference is most likely due to a lack of statistical convergence. From a physical perspective, Fig. 9 also suggests that the micro-jets have a strong effect on the turbulence structure. Indeed, the integral turbulence length scale $L_{uu}$ assessed from Fig. 9a, viz. along a line crossing the micro-jets is about twice smaller than what is obtained from Fig. 9b, viz. along a line where jets are not present. With a streamwise hole-to-hole distance of 11.68 $d$, the two assessments of $L_x$ are roughly 1.2 and 2.4 hole diameters. The same trend is observed from plots 9c and 9d.

### 3.2. *Cross-code comparison and flow structure*

As mentioned in Table 1, the discharge coefficient from the two 1-hole simulations from the two codes AVBP and CDP are very close, of order 0.66. Besides this agreement in the global parameter $C_D$, the two codes predict very similar jet structure. In both cases, the jet separates at the entry of the hole (Fig. 10, left column) and two different regions can be defined: the jetting region, near the upstream wall of the hole, where the jet shows high velocities, and the low-momentum region close to the downstream boundary of the hole. Note that because of the entrainment by the outer stream, the jet angle at the aperture outlet is somewhat different from the geometrical angle: it is approximately 28°, while the angle of the hole is 30°. As the length of the holes is small, the jet at the exit of the hole is still highly influenced by what happens at the entry of the hole. Figure 10 (right column) also shows that two counter-rotating vortices are present in the hole itself. Local asymmetries in the velocity field of the AVBP simulation are attributed to probable statistical convergence. The direction of rotation of these vortices is the same as for the classical counter-rotating vortex pair that is observed in jets in crossflow studies (see Andreopoulos & Rodi (1984)).

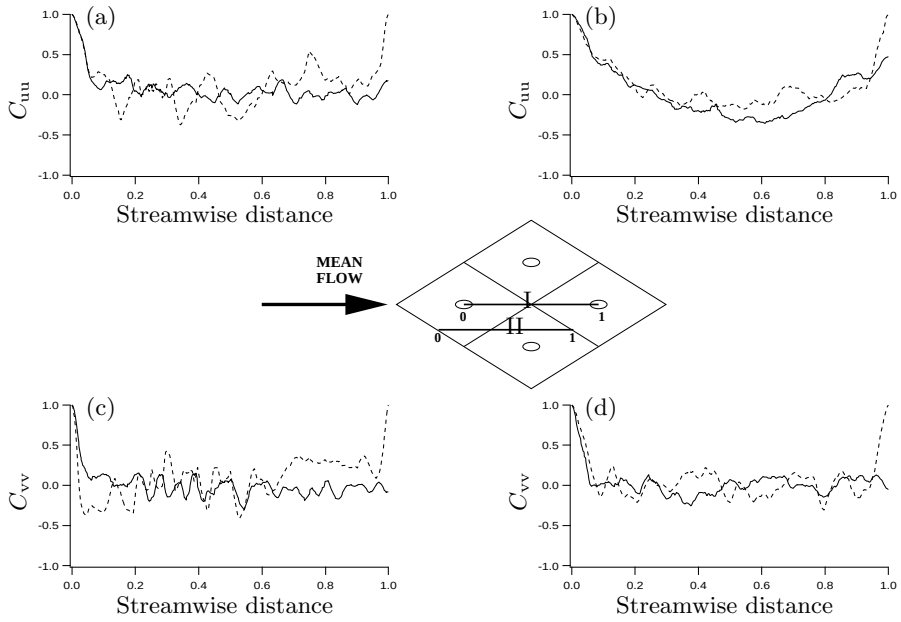


FIGURE 9. Streamwise two-point correlation coefficients for the streamwise [plots (a) and (b)] and normal [plots (c) and (d)] velocity from AVBP-1H (- - - - ) and AVBP-4H (——— ) at 1.2 diameter above the liner for paths I [plots (a) and (c)] and II [plots (b) and (d)]. The sketch between the plots depicts the paths along which the correlations have been computed.

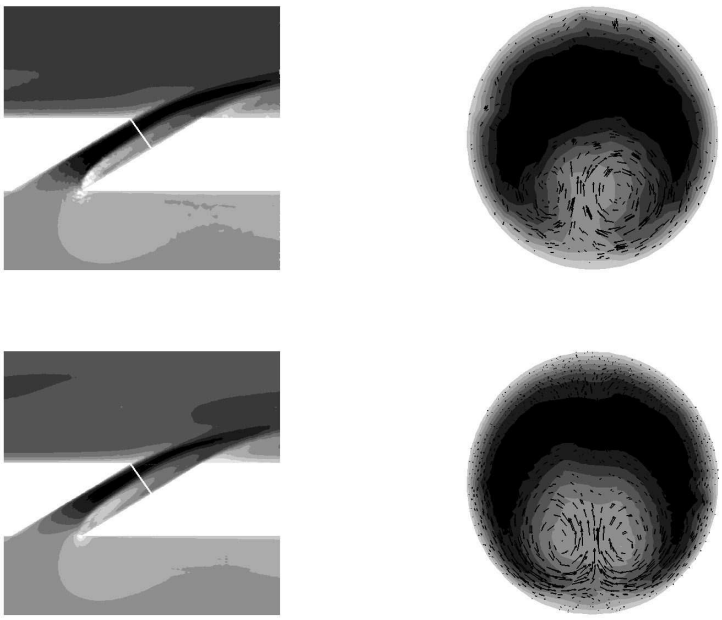

FIGURE 10. Computed mean streamwise velocity in the hole region. Top row: AVBP-1H, Bottom row: CDP-1H, Left column: Centerline plane, Right column: plane perpendicular to the jet flow (see white line in the left column). Scale is from $-0.18\ V_j$ (white) to $1.24\ V_j$ (black).

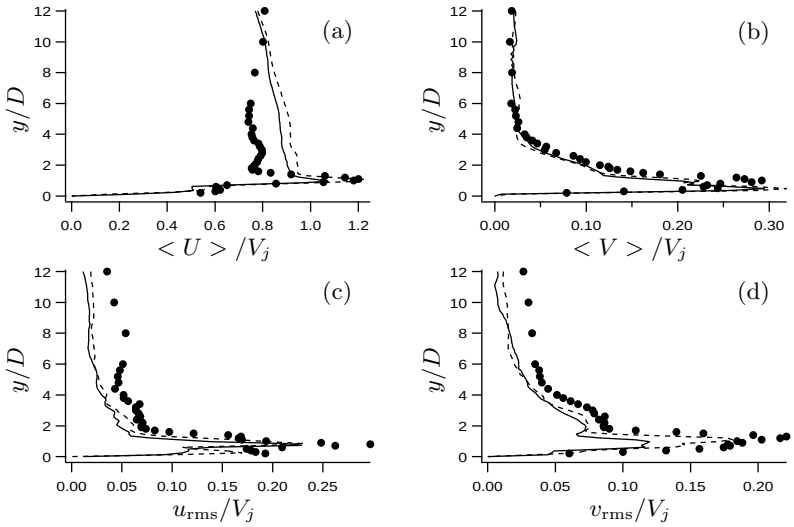


FIGURE 11. Velocity profiles from the "LARA" experiment (• ), the AVBP-1H (- - - - ) and CDP-1H (——— ) computations 2.92 diameters downstream of the hole: (a) time averaged streamwise velocity, (b) time averaged normal velocity, (c) rms of streamwise velocity, (d) rms of normal velocity.

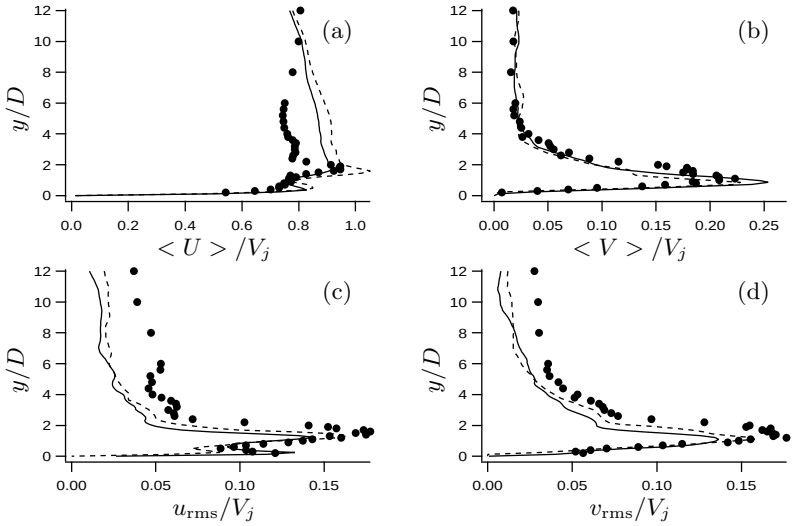


FIGURE 12. Velocity profiles from the "LARA" experiment (• ), AVBP-1H (- - - - ) and CDP-1H (——— ) computations 5.84 diameters downstream of the hole (viz. between two consecutive holes in the spanwise or streamwise direction): (a) time averaged streamwise velocity, (b) time averaged normal velocity, (c) rms of streamwise velocity, (d) rms of normal velocity.

Typical profiles from the 1-hole simulations performed with AVBP and CDP are compared in Figs. 11 and 12. The same locations as in Figs. 7 and 8 are used. The experimental data from Miron *et al.* (2005) are also reported. The overall agreement between the measurements and the AVBP and CDP calculations is very good.

## 4. Preliminary liner modeling

The ultimate goal of this ongoing work is to develop an equivalent model for the behavior of a multi-perfortated liner in turbulent flow. This model should, ideally, provide an accurate description of the mean flow and turbulence statistics of the coalesced film produced by the array of jets issuing from the holes in the liner. In this section we propose a simple model for the behavior of a multi-perforated liner and describe its numerical implementation. We present results from simulation of the coupled flow through parallel rectangular channels that communicate via the liner, in the configuration used in the "LARA" experiments.

### 4.1. *Formulation*

The present liner model is based on a simple description of the unsteady high Reynolds number flow through a circular aperture proposed by Howe (1979). This previous work was motivated by an interest in the interaction of acoustic waves with an aperture with a mean bias flow. However, the aperture model itself is incompressible, as the velocities in the vicinity of the aperture are generally small compared with the mean speed of sound. Howe obtained a linear relation between the fluctuating volume flow rate through the hole and the pressure fluctuations across it by hypothesizing an unsteady vortex sheet shed from the aperture rim. These vorticity fluctuations act as an acoustic sink and are convected away by the mean bias flow. Eldredge and Dowling (2003) developed a homogeneous liner acoustic impedance from this aperture model by smearing the mean aperture flow about the cell that encloses it. They found very good agreement between the model and isothermal acoustic experiments.

The success of the linear model in acoustic experiments demonstrates that it can successfully relate fluctuations in the through-flow of the liner to small pressure fluctuations in its vicinity. Furthermore, the basic principle of the model should also hold, even when these fluctuations are large. It has recently been shown by Luong *et al.* (2005) that the model is consistent with a non-linear model developed by Cummings (1983). The non-linear Cummings model, when specialized to cases in which the aperture flow does not reverse, is written as

$$l' \frac{\partial U_h}{\partial t} + \frac{1}{2\sigma^2} U_h^2 = \frac{1}{\rho} \Delta p, \tag{4.1}$$

where $U_h$ is the spatially average velocity through the aperture and $\Delta p$ is the pressure drop across the aperture. The constant parameters in the model are $\sigma$, the contraction coefficient of the issuing jet, and $l'$, a length scale that accounts for the inertia of fluid in and around the aperture. From consideration of the added mass of fluid adjacent to the aperture entrance and exit, then $l' = l_w + \frac{\pi}{2} a$, where $l_w$ is the physical thickness of the liner and $a$ is the aperture radius. Physically, the second term in Eq. 4.1 describes the loss of dynamic pressure as the jet emerges from the hole and mixes with the surrounding fluid. The unsteady term introduces a time lag due to fluid inertia.

These observations suggest that the model is a worthy candidate for describing a multi-perforated liner in turbulence simulations. We can follow a similar approach to Eldredge and Dowling (2003) to extend the aperture model (4.1) to a homogeneous liner. We suppose that the local normal velocity, $u_N$, is spatially distributed over the cell surrounding an aperture, so that

$$u_N = \alpha \, U_h, \tag{4.2}$$

where $\alpha$ is the porosity of the liner (defined as the total open area divided by the total

area of the liner). By conservation of mass, this through-flow velocity provides a Dirichlet condition for the flows on either side of the liner; in this case, the no-slip condition is enforced.

The interface model embodied in Eq. 4.2 gives no consideration to tilting of the apertures, nor the associated streamwise momentum that the discrete jets inject into the flow. These features are responsible for the film structure created by the coalescing jets. We therefore also propose a slightly more sophisticated model for both the normal and streamwise tangential velocity components,

$$u_N = \alpha U_h \sin\phi, \tag{4.3}$$

$$u_T = U_h \cos\phi, \tag{4.4}$$

for apertures of angle $\phi$ (where $\phi = \pi/2$ with no tilting). Note that the porosity is not used in the slip velocity component. The streamwise momentum flux in the jet is approximately $\rho U_h^2 A_h \cos\phi \sin\phi$, where $A_h$ is the cross-sectional area of the hole. From the modeled liner, the flux is $\rho u_N u_T A_c$ distributed over a cell of area $A_c = A_h/\alpha$. Relations 4.3 and 4.4 ensure that both mass and streamwise momentum flux from the homogeneous liner are equivalent to the discrete jets. In this model, we only enforce the slip velocity in Eq. 4.4 on the exit side of the liner; the no-slip condition is still enforced on the entrance side. This choice can be explored in future work. In the next section, we describe the implementation of this model in a full numerical simulation.

### 4.2. *Implementation*

The numerical implementation described here is focused specifically on a control volume-based collocated fractional-step method for computing incompressible flows on unstructured grids (Mahesh *et al.* 2004). However, its implementation can be generalized to other methodologies. There are two essential aspects of this implementation: stable integration of the aperture velocity model (4.1) and coupling of the two computational domains via this model.

Consistent with the interior scheme, we integrate Eq. 4.1 with a fractional step method:

$$\frac{\hat{U}_h - U_h^n}{\Delta t} = -\frac{1}{2\sigma^2 l'}\hat{U}_h^2 + \frac{1}{\rho}\frac{\Delta p^{n-1/2}}{l'}, \tag{4.5a}$$

$$\frac{U_h^* - \hat{U}_h}{\Delta t} = -\frac{1}{\rho}\frac{\Delta p^{n-1/2}}{l'}, \tag{4.5b}$$

$$\frac{U_h^{n+1} - U_h^*}{\Delta t} = \frac{1}{\rho}\frac{\Delta p^{n+1/2}}{l'}. \tag{4.5c}$$

Though this model nominally involves the "aperture velocity", the equations are treated as spatially continuous, and $U_h$ merely serves as an intermediate variable for the normal and tangential velocity components.

The pressure differences in this model require careful consideration. We take $\Delta p$ to be the difference in pressures immediately adjacent to each side of the liner, $\Delta p = p_2 - p_1$, where the subscripts refer to the computational domains, and $u_N$ is defined as positive when directed from 2 to 1. In the first substep, the pressures from the previous time step are used to advance the liner normal velocity. The intermediate liner velocity $\hat{u}_N$ is easily found as the sole physical root of the quadratic Eq. 4.5*a*. This velocity is enforced as a Dirichlet boundary condition (along with no-slip conditions in the tangent components) during the advancement of the first fractional step of the interior momentum equations.

Conservation of mass requires that the final substep (4.5$c$) must be considered in conjunction with the pressure Poisson equation formed from the corresponding substep in the interior. For any face adjoining two control volumes, the face-normal velocity component, $U_f$, obeys the following equation in the last substep:

$$\frac{U_f^{n+1} - U_f^*}{\Delta t} = -\frac{1}{\rho} \left. \frac{\partial p}{\partial n} \right|^{n+1/2}, \tag{4.6}$$

where $n$ is directed out of the volume. Local conservation of mass requires that the sum of the fluxes through the faces of each control volume must vanish at the end of the step. For interior control volumes, this leads to the following relation:

$$\sum_f \left. \frac{\partial p}{\partial n} \right|^{n+1/2} A_f = \frac{\rho}{\Delta t} \sum_f U_f^* A_f. \tag{4.7}$$

However, the flux through the face on the liner is determined by Eq. 4.5$c$ with either 4.2 or 4.3. Thus the overall pressure Poisson system is modified for control volumes along the liner. For example, for liner-adjacent control volumes in domain 1, using Eq. 4.3 to determine the normal velocity, we arrive at:

$$\sum_{f'} \left. \frac{\partial p}{\partial n} \right|^{n+1/2} A_f - \alpha \sin\phi \frac{p_1^{n+1/2}}{l'} A_f = \frac{\rho}{\Delta t} \left( \sum_{f'} U_f^* A_f - u_N^* A_f \right) - \alpha \sin\phi \frac{p_2^{n+1/2}}{l'} A_f, \tag{4.8}$$

where the sums are only taken over the interior faces.

Clearly, the pressure Poisson systems are coupled for domains 1 and 2 by the interface equations (4.8). To avoid having to solve these systems simultaneously, we utilize a staggered time approach:

($a$) For both domains, $U_h^n$ is used to provide the current interface conditions.

($b$) The pressure difference in the final substep is defined as $\Delta p^{n+1/2} = p_2^{n-1/2} - p_1^{n+1/2}$. The Poisson system in domain 1 is solved using the modified Eq. (4.8) with $p_2^{n-1/2}$, and $U_h^{n+1}$ is derived from the result using (4.5$c$).

($c$) Simultaneously, the Poisson system in domain 2 is solved with *no* modification.

($d$) At the end of these steps, the wall-normal velocity from domain 1 is exchanged with domain 2, and the liner pressure in domain 2 is exchanged with domain 1.

This approach ensures minimal latency of the parallel computations in each domain. Note that this algorithm can be iteratively corrected, with the last three steps alternated between the domains. However, the error after only a single iteration is of order $\Delta t$, which is consistent with the remainder of the fractional step methodology.

### 4.3. *A priori evaluation of model*

An initial evaluation of the liner model is presented in this section. Three hundred fields from the AVBP-1H run have been post-processed in order to compute the three terms of Eq. 4.1. Given the geometric characteristics of the perforated plate, the $l'$ length scale equals 23 mm while the contraction coefficient is considered to be equal to the discharge coefficient obtained in AVBP : $\sigma = C_D = 0.66$ (Table 1). The first idea was to compute the pressure drop $\Delta p$ in two different ways: as the difference between the mean pressure at the hole inlet and outlet ($\Delta p_h$), or as the difference between the mean pressure over the computational domain inlet and outlet ($\Delta p_\infty$). However, two reasons indicate that $\Delta p_\infty$ is a better candidate than $\Delta p_h$ to test the model of Eq. 4.1.

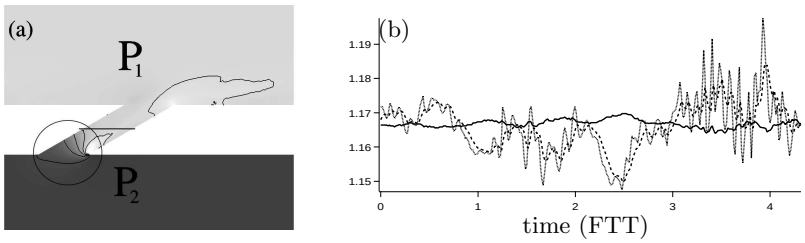


FIGURE 13. The liner model: *a priori* test from the AVBP-1H run **(a)**: Average pressure field on the centerline plane. **(b)**: Time evolution of the pressure drop post-processed from the AVBP-1H run: $\Delta P_\infty$ (——— ). Comparison with the pressure drop from Eq. 4.1, viz. $\rho l' \frac{\partial U_h}{\partial t} + \frac{\rho}{2\sigma^2} U_h^2$ (····· ) and with the pressure drop from Eq. 4.1 without the unsteady term, viz. $\frac{\rho}{2\sigma^2} U_h^2$ (– – – – ). All terms scaled by $\rho V_j^2$.

• The model proposed by Howe (1979) is based on variations of the external pressure far from the aperture, more represented by $\Delta p_\infty$.

• Figure 13a shows the pressure field on the centerline plane: at the hole inlet, the pressure is inhomogeneous: it varies from the far field pressure in the "cold" side $P_2$ to the far field pressure in the "hot" side $P_1$ in a very small region (see the circle in Fig. 13a).

The averaged velocity in the hole $U_h$ has been computed over a plane situated at half the thickness of the plate (shown by the horizontal line in Fig. 13a). In order to test the liner model, the pressure drop reconstructed from the $U_h$ signal by using Eq. 4.1 can be compared with the pressure drop directly computed from the AVBP-1H run.

The comparison is shown in Fig. 13b, which demonstrates that on the average, $\Delta p_\infty$ is well reproduced by the liner model (Eq. 4.1), even if the pressure fluctuations are overestimated. Still, the error between the pressure drop measured in the calculation and the one reconstructed from $U_h$ is never bigger than 4%. The term related to the inertia of the fluid introduces fluctuations in high frequencies but does not improve the model. Indeed the inertia of the fluid contained in the hole is not a first-order term in the liner model. Note that one can expect that these results would not hold if strong acoustic waves were impinging the liner.

### 4.4. *A posteriori evaluation of model*

In this section, we present the results of numerical simulations of a turbulent flow through parallel rectangular channels. A finite section of the common wall between the channels is composed of a multi-perforated liner, as can be seen in Fig. 3. In terms of the half-height of the channel, $h$, the width of the channel is $4h$, the entry length upstream of the liner is $12h$, and the length of the liner is $5.4h$. The liner extends across the entire width of the channel. These proportions are equivalent to the experiments conducted on the "LARA" test rig. The computational domain extends a further $12h$ units downstream of the end of the liner.

The simulations are conducted at centerline Reynolds number of 4000 and 2000 in the upper and lower channels, respectively. Note that these Reynolds numbers are approximately 4.5 times smaller than those used in the "LARA" experiments, and are chosen to ensure computational economy in this initial evaluation. A constant value is added to the pressure in the lower channel so that the mean pressure drop across the liner is 42 Pa. Periodic boundary conditions are used in the spanwise direction to suppress non-physical behavior at the junction between the liner and vertical side walls. The inlet velocity profiles in both channels are eighth-degree polynomials, randomly perturbed

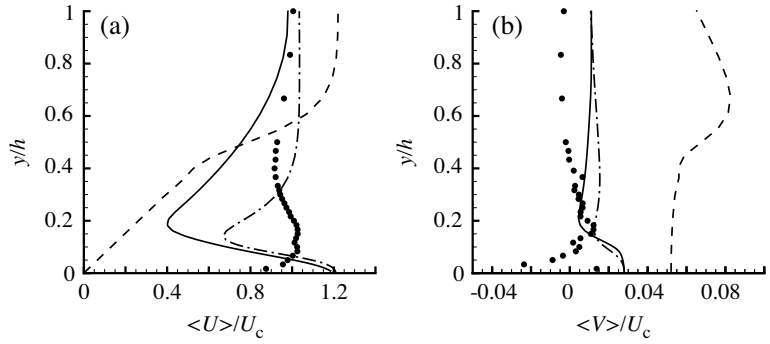


FIGURE 14. Mean velocity profiles in the (a) streamwise and (b) wall-normal direction. "LARA" experiment (• ); large-scale CDP simulation with liner normal velocity only and single channel (- - - - ); CDP with momentum flux and single channel (—·—); CDP with momentum flux and coupled channels (——— ).

with 10% perturbations. An orthogonal grid of $256 \times 64 \times 64$ is used in each channel, with grid stretching at the walls in the vertical direction, and in the vicinity of the upstream and downstream liner interfaces in the streamwise direction.

Three different versions of the liner model are evaluated by comparing them with the mean velocity profiles from the "LARA" experiments. In the first version of the model, only a wall-normal velocity is prescribed at the liner using Eq. 4.2, with no aperture tilting, while no-slip conditions are enforced in both tangential directions. In the second version, the momentum flux model (4.3)–(4.4) is applied. These first two versions are used in only a single channel with a uniform external pressure of 42 Pa. In the final version, the momentum flux model is applied to coupled channels. The results of these three versions are depicted in Fig. 14. Mean velocity profiles are evaluated along a vertical line across half of the upper channel, at 60% of the liner length. This position corresponds to the ninth row of holes in the physical liner. These profiles are compared with the experimental profiles, which have been spatially averaged from a number of sample locations in the vicinity of an aperture.

From the comparison in Fig. 14, it is clear that simply enforcing a wall-normal velocity condition is insufficient for creating a film-like flow near the wall. When streamwise momentum is also injected into the domain, a thin layer is created near the wall, but this layer fails to mix with the bulk flow in the channel as it does in the experiments (though it should be noted that the low Reynolds number and undeveloped inlet flow leads to a primarily laminar flow with poor mixing). There is also a striking difference between the single channel and coupled channel results, indicating the significance of computing the flow in the "driving" channel. The vertical velocity profiles also disagree with experiments, though the negative wall values observed in the experimental results indicate errors in averaging a limited number of profiles.

The importance of simulating the coupled interaction of two domains is emphasized by the results in Fig. 15. This figure displays the mean profiles of vertical velocity at several streamwise locations. As expected, this velocity component is continuous across the liner interface. However, its profile reveals significant variation from the lower channel to the upper. Fluid is drawn upward in the lower channel for most of the length of the liner, but the strong streamwise velocity and lack of turbulent mixing along the liner in the upper channel confines the upward momentum to a thin layer. Furthermore, the vertical

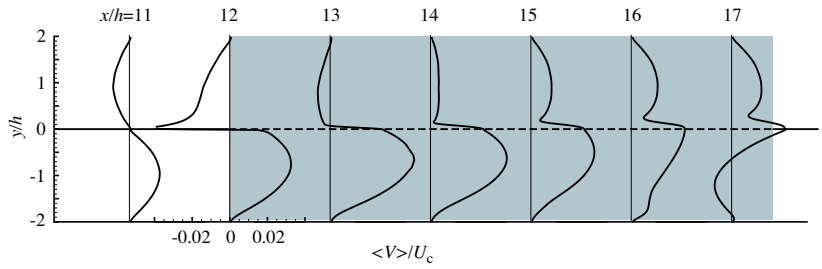


FIGURE 15. Profiles of vertical velocity across coupled channels, at several streamwise locations, from large-scale CDP simulation. Position of liner is indicated by gray background.

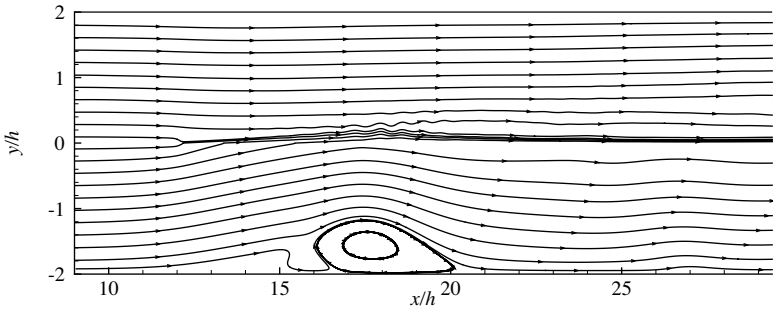


FIGURE 16. Mean streamline pattern for coupled channels.

velocity reverses sign in the lower portion of the lower channel, near the downstream end of the lined section. This behavior is due to a separation bubble that resides on the bottom wall of this channel, as seen in the mean streamline plot in Fig. 16. As fluid leaves the lower channel for the upper, it leaves a region of weakened pressured below the liner and, consequently, an adverse pressure gradient is set up in the lower channel.

Small ripples in the streamline pattern are also apparent just above the liner in Fig. 16. These reflect a shear flow instability that initially develops at the downstream edge of the liner and then roots itself at the middle of the liner. The streamwise velocity profile in Fig. 14a created by the interface model likely admits such instabilities, though no analysis is attempted here. More importantly, the liner interface model presented here leads to flow phenomena that are not apparent in the experiments.

Evaluation with higher Reynolds numbers and better developed turbulent inlet flow would provide a clearer demonstration of this model's effectiveness. However, these simulations have revealed fundamental limitations of a model confined to the interface. The structure of an effusion film created by coalescing discrete jets depends on the interaction of these jets with the ambient flow. It is not possible to rely exclusively on a homogeneous injection of an equivalent amount of mass and momentum to generate a similar film structure. This suggests adopting a non-local approach, for example by using distributed forcing in the mass and momentum equations. This is the subject of a current investigation.

## 5. Conclusions

The code-to-code, experiments-to-simulations, and domain-to-domain comparisons show that wall-resolved LES can capture the essential characteristics and statistics of the tur-

bulent flow with effusion. The related computing effort can be reduced significantly by using a single-hole bi-periodic computational domain since jet-to-jet interaction does not seem to occur, at least for the operating points considered. This opens new perspectives in terms of generating relevant data for supporting the development of wall models relevant to effusion cooling applications. A preliminary model for the multi-perforated liner has been presented, and *a posteriori* testing has been conducted with the configuration of the "LARA" experimental rig. A robust algorithm has been developed to integrate the dynamic model in a mass-conservative manner, and to efficiently couple the computational domains that share the liner at their interface. The results reveal that the model is insufficient for providing the equivalent structure of an effusion film produced by discrete jets. A more sophisticated approach will be pursued in future work.

## Acknowledgments

The authors gratefully acknowledge support from CINES for the computer resources and the European Community for participating in the funding of this work under the project INTELLECT-DM (Contract No. FP6 - AST3 - CT - 2003 - 502961).

## REFERENCES

Andreopoulos, J. & Rodi, W. 1984 Experimental investigation of jets in a crossflow. *J. Fluid Mech.* **138**, 93–127.

AVBP 2006 AVBP Code: www.cerfacs.fr/cfd/avbp_code.php and www.cerfacs.fr/cfd/CFDPublications.html

Cummings, A. 1983 Acoustic nonlinearities and power losses at orifices. *AIAA J.* **22** (6), 786–792.

Eldredge, J. D. & Dowling, A. P. 2003 The absorption of axial acoustic waves by a perforated liner with bias flow. *J. Fluid Mech.* **485**, 307–335.

Goldstein, R. J. 1971 Film Cooling. In *Adv. Heat Transfer* **7**, 321–379 . Ed. Academic Press, New York and London.

Ham, F. & Iaccarino, G. 2004 Energy conservation in collocated discretization schemes on unstructured meshes. In *Annual Research Briefs 2004*, Center for Turbulence Research, NASA Ames/Stanford Univ.

Howe, M. S. 1979 On the theory of unsteady high Reynolds number flow through a circular aperture. *Proc. Roy. Soc. Lond. A* **366**, 205-223.

Lefebvre, A. H. 1999 *Gas Turbines Combustion*. Taylor & Francis.

Luong, T., Howe, M. S. & McGowan, R. S. 2005 On the Rayleigh conductivity of a bias-flow aperture. *J. Fluid Struct.* **21**, 769–778.

Mahesh, K., Constantinescu, G. & Moin, P. 2004 A numerical method for Large-eddy simulation in complex geometries. *J. Comp. Phys.* **197**, 215-240. CTR04.

Mendez, S., Nicoud, F. & Miron, P. 2005a Direct and large eddy simulations of a turbulent flow with effusion. In *ERCOFTAC Workshop - DLES6*. Poitiers, France.

Mendez, S., Nicoud, F. & Poinsot, T. 2005b Large-eddy simulation of a turbulent flow around a multi-perforated plate. In *CY-LES*. Limassol, Cyprus.

Miron, P., Mendez, S., Nicoud, F. & Bérat, C. 2005 Comparison between lda measurements and LES predictions of cold airflows through a multi-perforated plate. In *Numerical Heat Transfer 2005 EUROTHERM Seminar 82*. Gliwice-Cracow, Poland.

Yavuzkurt, S., Moffat, R. J. & Kays, W. M. 1980 Full coverage film cooling. Part 1. Three-dimensional measurements of turbulence structure. *J. Fluid Mech.* **101**, 129–158.